INTERFACE

rsif.royalsocietypublishing.org

Research

Cite this article: Filippidi E, DeMartini DG, Malo de Molina P, Danner EW, Kim J, Helgeson ME, Waite JH, Valentine MT. 2015 The microscopic network structure of mussel (*Mytilus*) adhesive plaques. *J. R. Soc. Interface* **12**: 20150827.
http://dx.doi.org/10.1098/rsif.2015.0827

Received: 17 September 2015
Accepted: 10 November 2015

Subject Areas:
biomaterials, biophysics

Keywords:
mussels, *Mytilus*, plaques, small-angle neutron scattering, electron microscopy

Author for correspondence:
Megan T. Valentine
e-mail: valentine@engineering.ucsb.edu

Electronic supplementary material is available at http://dx.doi.org/10.1098/rsif.2015.0827 or via http://rsif.royalsocietypublishing.org.

THE ROYAL SOCIETY PUBLISHING

The microscopic network structure of mussel (*Mytilus*) adhesive plaques

Emmanouela Filippidi[1], Daniel G. DeMartini[2], Paula Malo de Molina[3], Eric W. Danner[4], Juntae Kim[3], Matthew E. Helgeson[3], J. Herbert Waite[1,2,4] and Megan T. Valentine[1,5]

[1]Materials Research Laboratory, [2]Molecular, Cellular and Developmental Biology, [3]Chemical Engineering, [4]Biomolecular Science and Engineering, and [5]Mechanical Engineering, University of California Santa Barbara, Santa Barbara, CA, USA

EF, 0000-0002-4044-0022; PMdM, 0000-0002-9911-5320; EWD, 0000-0003-4630-1100; JK, 0000-0002-1319-3521; MEH, 0000-0001-9384-4023; MTV, 0000-0003-4781-8478

Marine mussels of the genus *Mytilus* live in the hostile intertidal zone, attached to rocks, bio-fouled surfaces and each other via collagen-rich threads ending in adhesive pads, the plaques. Plaques adhere in salty, alkaline seawater, withstanding waves and tidal currents. Each plaque requires a force of several newtons to detach. Although the molecular composition of the plaques has been well studied, a complete understanding of supra-molecular plaque architecture and its role in maintaining adhesive strength remains elusive. Here, electron microscopy and neutron scattering studies of plaques harvested from *Mytilus californianus* and *Mytilus galloprovincialis* reveal a complex network structure reminiscent of structural foams. Two characteristic length scales are observed characterizing a dense meshwork (approx. 100 nm) with large interpenetrating pores (approx. 1 µm). The network withstands chemical denaturation, indicating significant cross-linking. Plaques formed at lower temperatures have finer network struts, from which we hypothesize a kinetically controlled formation mechanism. When mussels are induced to create plaques, the resulting structure lacks a well-defined network architecture, showcasing the importance of processing over self-assembly. Together, these new data provide essential insight into plaque structure and formation and set the foundation to understand the role of plaque structure in stress distribution and toughening in natural and biomimetic materials.

1. Introduction

Marine mussels living in the intertidal zones off the California coast, such as *Mytilus californianus* (Conrad, 1837) and *Mytilus galloprovincialis* (Lamark, 1819) are continuously subjected to waves and tidal currents which threaten to dislodge them [1] from the rocks they are attached to and their colonies. To maintain a robust connection to rocks and to each other, every mussel creates hundreds of attachments, collectively termed the *byssus*. The extraordinary ability of the byssus to bind to a variety of pristine and bio-fouled surfaces (e.g. glass, metal, plastic) in a matter of minutes while immersed in the high salt and basic pH conditions imposed by seawater has attracted the attention of many researchers and resulted in the creation of biomimetic glues for medical and broader use [2–6].

To date, however, most bioinspired adhesives mimic the molecular biochemical properties of plaque-derived proteins, without regard to the unique structural features of the byssus that enhance adhesive strength. Such features include the byssal threads, thin and extensible [7] collagen-reinforced fibres, connected to a flat and wide plaque into which the collagen microfibrils penetrate. Each plaque–thread system exhibits strong plaque–substrate adhesion with a detachment force approximately 2 N as measured upon quasi-static tension [8]. For a typical byssus of a *Mytilus* consisting of 50 or more plaques [9], tens of newtons are required to dislodge a mussel from a surface. One important contribution

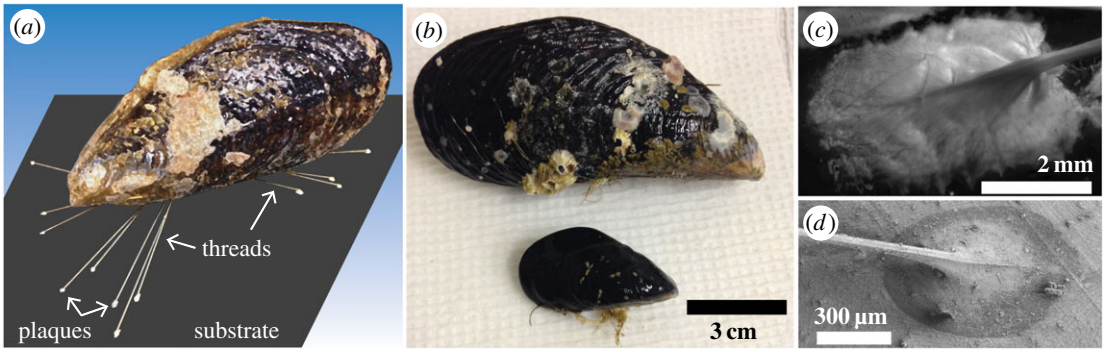

Figure 1. (*a*) Schematic of a mussel attached on a surface via threads ending in plaques. (*b*) Typical mussels used for this study: *M. californianus* (top) and *M. galloprovincialis* (bottom). (*c,d*) *M. californianus* plaque with visible thread junction deposited at 19°C (*c*) on glass by the typical largest mussel of length 11.5 cm (stereo image) and (*d*) on aluminium foil by the smallest mussel of length 2 cm (SEM image). Plaque size scales with mussel size for the case of *M. californianus*. (Online version in colour.)

to mussel plaque tenacity arises from the molecular-scale interfacial adhesion of the mussel foot proteins (mfps), which have adhesion energies on the order of 10 mJ m^{-2} as measured by the surface forces apparatus [10,11]. However, this interfacial adhesion alone cannot explain the fracture energy required to dislodge an entire plaque from a glass surface, which is measured to be of the order of 10^5 mJ m^{-2} [8]. Thus, the enhanced strength of the structure relies on the ability of the plaque and thread to dissipate and distribute energy within the bulk, rather than at the interface alone.

Strong adhesion also requires excellent cohesive strength to ensure that the structures do not fail by internal tearing under load. Plaque cohesion has been shown to partly arise from enhanced hydrogen bonding and metal coordination enabled by the abundant catecholic side groups of 3,4-dihydroxyphenyl-L-alanine (DOPA) in the mfps [12] in conjunction with catechol oxidase-mediated protein cross-linking [13]. Mussel foot proteins mfp-1, -2, -3, -4, -5, -6 have been purified and extensively studied and mfps-1, -2 and -3 have been shown to be intrinsically disordered or have disordered domains [14] with possible advantages for plaque processing and assembly. The role of these proteins in energy dissipation is not yet understood. A possible explanation may arise not from the molecular-level protein interactions, but from the supramolecular structures of the byssus at the micrometre scale, which is the focus of this work. Through a quantitative study of mussel plaque architecture of two *Mytilus* species, we establish and characterize the unique structures of the plaque. Our results provide new insight into the natural design of biological adhesives as well as the engineering requirements for the design of improved bioinspired adhesive structures.

2. Material and methods

2.1. Natural plaques

We examined two species of marine mussels commonly found along the California coast, *M. californianus* (typical adult length ≈ 10 cm) and *M. galloprovincialis* (typical adult ≈5 cm) (figure 1*b*). Mussels were collected from the intertidal zone off the coast of Santa Barbara, CA, and placed in tanks with continuously circulating filtered seawater. Tied to acrylic (Plexiglas®) plates, mussels formed their byssus at the physiologically relevant water temperature of 19°C. For studies of temperature-dependence, a random selection of mussels was placed in a cold room at 3.8°C with daily changes of seawater. For all mussels, every 2 days, the byssal distal end was collected by separating the plaque from the acrylic with a razor blade; plaques were separated from threads using dissecting scissors. To preserve their structure, plaques and threads were fixed overnight at room temperature using 3.7% formaldehyde solution in water and subsequently stored at 6°C for 2 days until immersion in deuterium oxide (D_2O, 99.9%, Cambridge Isotope Laboratories) for at least 3 days in preparation for neutron scattering. In the case of *M. californianus*, the mussels exhibited a large size variation that allowed us to explore the effects of mussel size on plaque structure. To assess the dependence on size, the typical mussels of length $L = 11.5$ cm used for all other experiments were tied on aluminium foil-covered plates alongside smaller, younger mussels of $L = 2.0$, 2.6 and 5.6 cm, producing plaques of areas $A \approx 0.17$, 0.4, 2 and 12 mm^2 (figure 1*c–d*). To study the effect of protein denaturation on the supra-molecular assembly, the 19°C plaques were immersed post-collection in 6 M guanidine hydrochloride in D_2O, the standard chaotropic salt for protein denaturation (GuHCl, Sigma G3272).

2.2. Induced plaques

Dissected *M. californianus* were induced by injection of 0.56 M KCl in H_2O at the pedal ganglion following the procedure described by Tamarin *et al.* [15] at room temperature. We positioned a coverslip over the distal depression to mimic the natural attachment the mussel would make to a surface. Within minutes of the induction, the induced plaque appeared as a turbid, creamy material at the distal depression of the foot (electronic supplementary material, figure S1). The induced plaque and partial thread were attached on the coverslip, which we carefully removed from the foot, avoiding any contact with the induced material. Induced plaques were collected at three time points: $t = 0$ (time of first appearance), 10 and 30 min. To examine the physiological effect of basic seawater (pH ≈ 8) compared to the acidic pH at the distal depression, identical preparation of induced plaques was submerged in seawater for 5 min after collection and before fixation. Induced plaques were fixed in 3.7% formaldehyde solution in water overnight and stored at 6°C until immersion in D_2O.

2.3. Neutron scattering

Small-angle and ultra-small-angle neutron scattering (SANS and USANS) were carried out at the NIST Center for Neutron Research (Gaithersburg, MD, USA). SANS was performed at the 30 m NG7 beamline and USANS at the BT5 beamline, covering a q-range 3.33×10^{-5} to 0.5 $Å^{-1}$. For the detector distances of 1, 4 and 13.5 m, the wavelength was $\lambda = 6$ Å ($\Delta\lambda/\lambda = 11\%$) and for the 15.3 m with lenses, $\lambda = 8.09$ Å. For the USANS measurements, $\lambda = 2.4$ Å ($\Delta\lambda/\lambda = 6\%$). Plaques were manually placed in the 1 mm thick titanium scattering cells with transparent quartz windows. The 10CB sample environment was used with the temperature set at 22°C. Empty cells were used in the determination of

background. Whereas the SANS data were two-dimensional and was radially averaged, the USANS data were vertically averaged at the detector producing a one-dimensional dataset. No multiple scattering was observed, with transmissions in the SANS regime ranging from 0.7 to 0.85. Data were reduced using the NCNR Igor procedures [16]. Fitting was performed with the SASfit package (v. 0.94.2) maintained by the Paul Scherrer Institute [17]. The incoherent background was determined at high q assuming a Porod scaling, set as a constant and subtracted from the experimental data.

2.4. Scanning electron microscopy

Plaques were embedded in Neg-50 cryoprotectant (Thermo Sci.) at −21°C and sectioned using a cryostat (Leica CM1850) in 14 µm thick sections which were immediately placed in milli-Q water. After multiple milli-Q rinses to remove the embedding medium, solvent exchange from water to ethanol to hexamethyldisilazane (HMDS, CAS 999-97-3) was performed, in steps of water : ethanol 3 : 1, 1 : 1, 1 : 3, 1 : 9, 0 : 1 (×3), and ethanol : HMDS 2 : 1, 1 : 2, 0 : 1 (×2). Samples were sputter coated with gold/palladium 60/40, 99.99% (Hummer 6.2, Anatech, USA) for 90 s and imaged in secondary electron mode with a scanning electron microscope (FEI XL30 Sirion FEG) using accelerating voltages of 2–3 kV to avoid damaging the proteinaceous samples. Both formaldehyde-fixed and unfixed plaques resulted in identical imaging results. Pore sizes were quantified via image analysis, by measuring the major and minor axis in ImageJ ($n = 66–202$ per section). For the comparison among different sized plaques, the *M. californianus* mussels described in §2.1 were used. For the comparison of sections along the plaque's long axis, plaques from the mussel of length $L = 11.5$ cm were used.

3. The structure of natural plaques

3.1. Imaging of natural plaques

Scanning electron microscopy (SEM) is a powerful tool for studying the features of plaques, which are of the order of tens of nanometres to micrometres. This is in contrast to transmission electron microscopy where the small sample thickness required does not allow for the imaging of the full structure (plate 1 of Tamarin *et al*. [15]) hindering a clear interpretation. SEM images of freeze-dried plaques were previously reported to have an outer cuticle of ≈20 µm thickness protecting a 'foamy' interior, composed of large micrometre-sized pores embedded in a continuous mesh network (fig. 4 of Lee *et al*. [12]). However, since freeze-drying is known to disrupt soft structures [18], we employ a gentler method of preparation: incremental solvent exchange from water to ethanol to HMDS, which is known [19] to result in equal structural preservation as critical point drying.

The resulting images (figure 2 and electronic supplementary material, S2), which reveal almost identical structures for both species studied, reaffirm the existence of the large micrometre-diameter pores, reveal a thinner cuticle, but also exhibit the previously underestimated extent of the mesh network. Whereas previously the collapsed struts appeared so bent that it was thought they were protein aggregates with little void space in between them, it is now clear that a network of straight, fine diameter (100 nm) struts occupies a large volume fraction, containing voids that in the wet environment are presumably filled with water or physiological fluid. The appearance of this network is reminiscent of reticulated foams such as nickel [20] or Al_2O_3 and the resemblance in

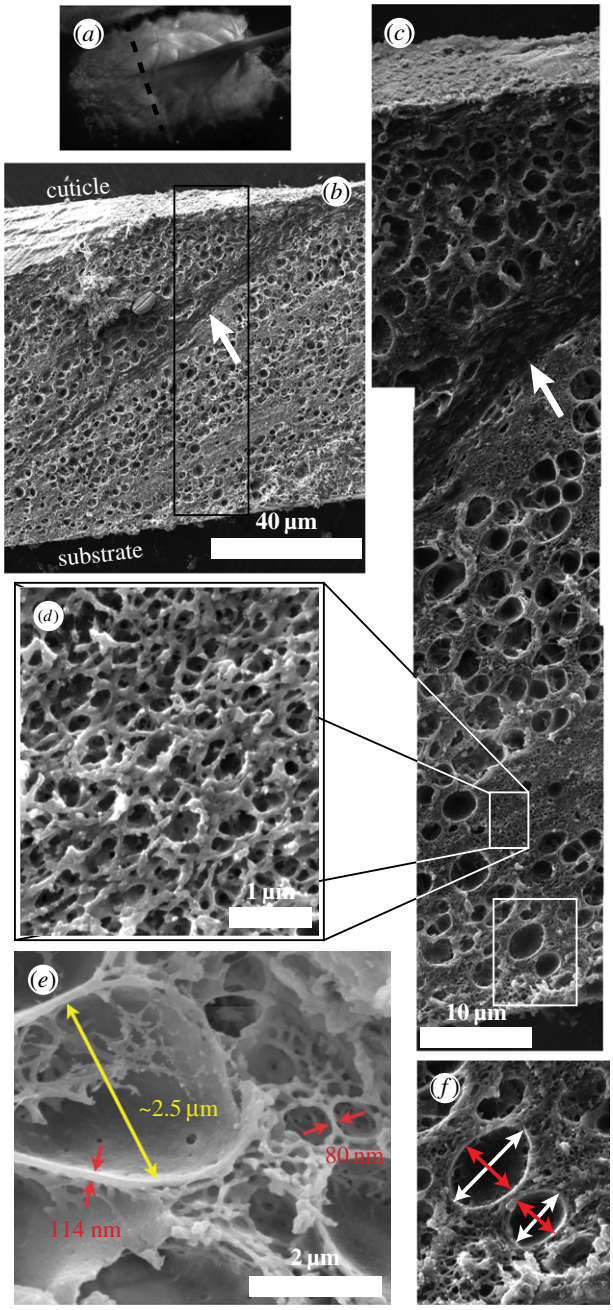

Figure 2. (*a*) Stereo microscope image of a *M. californianus* plaque formed at 19°C and the location of the cross-section. (*b–f*) SEM images of cross-sections. (*b*) View with protective cuticle visible at the top and interpenetrating collagen thread (arrow) splaying from the thread at the top right and penetrating diagonally into the plaque. (*c*) Image of the boxed section in (*b*) where the collagen (arrow) and the larger pores are visible. (*d*) Zoomed in view of the reticulated mesh network. (*e*) Clearly visible are the polymer struts inside the pores. (*f*) Zoomed in view of the pores and example of the major (white) and minor (red) axes of the pores. (Online version in colour.)

strut persistence length and connectivity raises questions about their load-bearing and load-distribution significance. The gentler solvent exchange preparation also reveals a network inside the large pores, which under the freeze-drying conditions appeared mostly empty. Thus, we conclude that this inner network is more fragile compared with the outer mesh network and may not be suitable for load-bearing, but rather a remnant of a protein aggregation process. Through careful examination of tens of fields of view within the same plaque, cross-sections at various plaque locations belonging

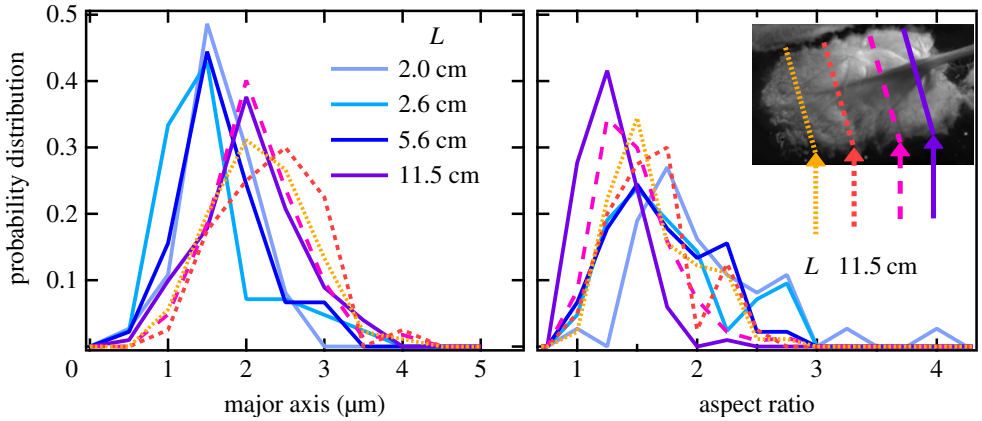

Figure 3. Probability distribution functions of the major axis and aspect ratio of the pores for differently sized mussels (solid lines) and different locations (dashed lines) within the plaque originating from the $L = 11.5$ cm mussel. (Online version in colour.)

to many different mussels, we determine the existence of two microscopic length scales arising from five different sources: (*a*) the diameter of the branches of the outer mesh network falls in the range of 75–100 nm; (*b*) the separation between opposing branches is hundreds of nanometres, but less than 1 μm; (*c*) the diameter of the branches of the inner pore network, in the range of 90–120 nm; (*d*) the walls of the large pores with thickness in the 90–130 nm range; and (*e*) the diameter of the pores in the micrometre scale 1.5–2.5 μm. The five groups can be grouped into two: one group encompassing the walls and struts largely falling in the 75–130 nm range and another group for the diameter of the large pores in the 1–3 μm range.

The SEM images from *M. californianus* plaques are further analysed to determine the distribution of pore sizes within the plaque and whether pore size is correlated with mussel length or plaque area. The probability distribution functions of the major axis and the aspect ratio are shown in figure 3. For the three smallest mussels with lengths $L = 2.0$, 2.5 and 5.6 cm, the mean $\pm$ standard error (s.e.) are comparable, with the major axis values being 1.67 ± 0.08 μm, 1.54 ± 0.10 μm and 1.64 ± 0.07 μm, respectively, whose ranges overlap. To quantitatively compare the distributions, we use the Kolmogorov–Smirnov (KS) two-sample non-parametric test at a significance level $\alpha = 5\%$. We find no statistically significant difference among the three distributions (p-values approx. 0.98) in all possible permutations.

For the largest mussel ($L = 11.5$ cm), it is possible to examine the pores measured in different cross-sections along the length of the plaque. We find that the distributions largely overlap with means $\pm$ s.e. from front to back: 2.15 ± 0.06 μm, 2.3 ± 0.1 μm, 2.13 ± 0.04 μm and 2.03 ± 0.06 μm. The KS test shows no statistically significant difference with p-values approximately 0.98. For plaques derived from the largest mussel, there is a modest shift in the distribution compared with the smaller mussels. However, the difference is not statistically significant (p-values approx. 0.96). It is important to note that all samples have appreciable polydispersity arising both from natural variability of the pores and from the sectioning which cuts through off-centre distances. If the pores were completely spherical, the spheric sections would exhibit an aspect ratio of 1. However, the overall aspect ratio of 1.56 ± 0.02 points to elongated but not rod-like structures, exactly as visualized. Finally, although we doubt any correlation of the major axis' direction with the sectioning direction imposed in the cryostat, we cannot completely rule it out.

The lack of scaling of the pore diameter with mussel size, coupled with our observation that a fragile polymer network exists within the pores, hints at possible origins of this unique structure: the pores may be remnants of the mfp-containing phenol granules that participate in plaque formation and are of similar size ($\approx$1 μm) to the observed pores [15] or the pores may be the result of cross-linking of the transient coacervate phase which occurs due to the mixing of oppositely charged mfp polyelectrolytes during plaque deposition. Recent evidence [21] supports coacervate formation by one variant (mfp-3s) of the mfp family. In this case, the observed pores may be the solidified interface of the mfp-poor liquid drops dispersed in an mfp-rich continuous phase corresponding to the mesh network. The second possibility not only raises important questions with regard to biological structure formation, but suggests new routes to the design of synthetic materials with particular micro-scale architecture by controlling phase transitions or phase separation. Soft foam-like architectures of adhesive structures have also been reported for marine organisms such as the buoy barnacle's (*Dosima fascicularis*) cement used for floating [22] and the sandcastle worm's (*Phragmatopoma californica*) tube cement used to connect sand and pebbles for its tubular shells [23]. While the former is hypothesized to be created by a distinctly different mechanism using carbon dioxide-filled bubbles, the latter is proposed to emerge from coacervate phase inversion, cross-linking and solidification [24], a possibility for the mussel. However, no evidence of a mesh network is reported for *P. californica*, differentiating it from the *Mytilus* plaque. Other materials, like the cuttlefish's bone, are similarly cellular structures, but are non-adhesive, load-bearing, hard, mineralized gas-filled materials, pointing to the many forms and functions of cellular materials in marine organisms.

3.2. Scattering of natural plaques

To complement the SEM imaging, which only provides a local view of the structure after solvent exchange treatment, we employed a combination of SANS and USANS on assemblies of more than 20 whole plaques under wet conditions, providing a statistically meaningful ensemble. As shown in figure 4, the combined profiles of the background-corrected coherent scattered intensity, I_{coh}, versus the scattering vector, q, do not exhibit any clearly identifiable peaks corresponding to a particular spacing, nor point to a strong structure factor.

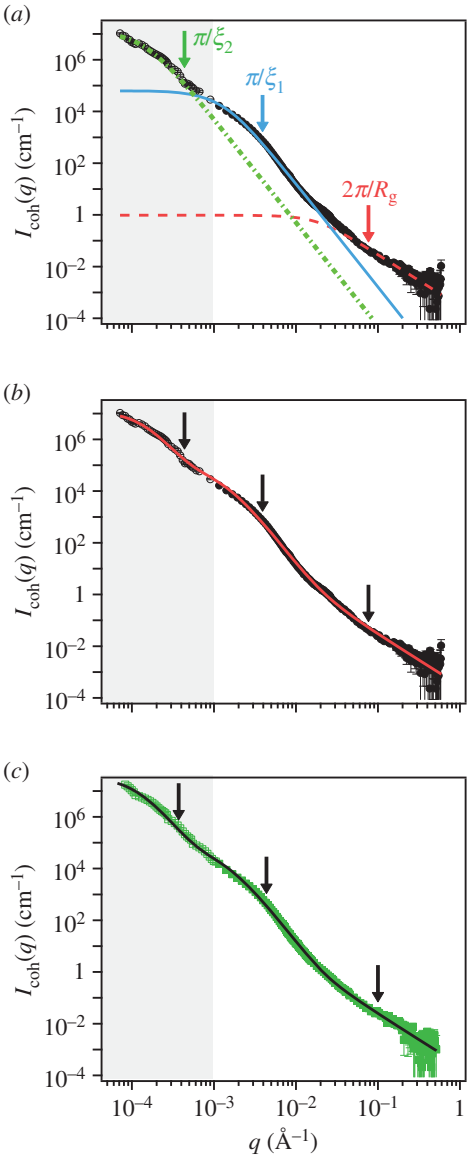

Figure 4. SANS ($0.001 < q < 0.58$ Å^{-1}) and USANS (grey, $7 \times 10^{-5} < q < 9 \times 10^{-4}$ Å^{-1}) scattering intensity for the natural plaques made at 19°C. Lines represent the model fit and arrows (from left to right) indicate π/ξ_2, π/ξ_1 and $2\pi/R_g$. (*a*) *M. californianus*. Lines represent the three individual contributions to the fit (3.1): random coil (dashed red), DAB model ξ_1 (solid blue) and DAB model ξ_2 (dotted green). (*b*) *M. californianus* with complete fit. (*c*) *M. galloprovincialis* with fit. (Online version in colour.)

This is consistent with the polydispersity of the pore sizes and the variety of branch lengths and radii observed by SEM. The scattering curves are composed of three regions, a low q region with power law decay $q^{-2.4}$, a middle q region where the power law changes to $q^{-4.1}$ and a high q regime with a power law of q^{-2}. We do not observe signatures of cylindrical branches expected from the mesh network, such as consecutive minima or a q^{-1} power law characteristic of cylinders. Cylindrical network junctions displaying a q^{-2} decay in the mid-q regime followed by a plateau at low-q [25] are also not observed. Hammouda [26] has shown that the form factor of branched polymers exhibits a broad shoulder and a decay with q^{-c}, $2 \leq c \leq 1$, again incompatible with our experimental curves. Rather, the q^{-4} scaling suggests the dominance of scattering from interfaces.

Based on this, we choose to model the scattering as the summation of two Debye–Anderson–Brumberger (DAB) terms, accounting for interfacial scattering from surfaces with a discontinuous scattering length density [27,28], in addition to a random coil term I_{RC} describing the protein configuration at the highest q values.

$$I_{coh}(q) = I_{RC}(q) + \frac{I_1}{(1+(q\xi_1)^2)^2} + \frac{I_2}{(1+(q\xi_2)^2)^2}, \qquad (3.1)$$

with arbitrarily chosen $\xi_1 < \xi_2$.

The interfacial contribution to scattering at both moderate and low q suggests two characteristic length scales, indicated by shoulders in the scattering in the respective regions of the profiles. This agrees with the SEM results of two dominant length scales and suggests that the SEM sample preparation preserves the natural structures. The network can be regarded as a combination of large pores and thin struts (and walls) with characteristic length scales separated by roughly an order of magnitude. The best fit and the three individual contributions in the fit are shown in figure 4. For the *M. californianus* plaques (figure 4), best fits occur for $\xi_1 = 78.8 \pm 0.6$ nm and $\xi_2 = 0.71 \pm 0.01$ µm, while for *M. galloprovincialis* $\xi_1 = 73.2 \pm 0.5$ nm and $\xi_2 = 0.86 \pm 0.01$ µm.

The best fit ξ_1 values in the mid-q regime are in excellent agreement with the SEM-measured strut and wall thicknesses. However, the scattering ξ_2 values fall at the lower end of the pore size distributions reported in figure 3. Scattering from the pores of diameter 1–3 µm is superimposed with scattering from the smaller mesh network voids of length ℓ, $80 < \ell < 1000$ nm, increasing polydispersity and driving the average contribution to higher q values. In addition, the fit may be capturing a smaller length scale than the expected one, as the fit assumes a convergence of $I_{coh}(q \to 0)$ to a plateau, but the data are not exhibiting a plateau within the experimental range. Possibly additional larger length scales are present, arising from the collagen fibres or from gaps between the plaques' positions.

Scattering at high q values relates to the internal configuration of the proteins comprising the plaque. We use the Flory polymer theory to relate scattering to structure where I_{RC}, the generalized Gaussian coil contribution, is described by

$$I_{RC}(q) = \frac{I_0}{\nu U^{1/\nu}}\left[U^{1/2\nu}\Gamma\left(\frac{1}{2\nu}\right) - \Gamma\left(\frac{1}{\nu}\right) - U^{1/2\nu}\Gamma\left(\frac{1}{2\nu}, U\right) + \Gamma\left(\frac{1}{\nu}, U\right)\right], \qquad (3.2)$$

where

$$U = \frac{2\nu+1}{2\nu+2} q^2 \frac{R_g^2}{6}, \qquad (3.3)$$

where $\Gamma(x)$ is the Gamma function, R_g the Guinier radius and ν the Flory exponent. Flory theory relates R_g to N, the number of Kuhn segments, which for proteins is regarded to be the number of amino acids [29], giving $R_g \sim N^{\nu}$. υ is 1/3 for a spherical globule, 1/2 for a random coil (theta solvent) and 3/5 for an excluded volume polymer in good solvent. The latter has been refined by renormalization group methods to $\upsilon = 0.588$ [30]. In the plaque, we do not expect the proteins to behave as if they were fully solvated polymers or denatured proteins, as there is a large degree of cross-linking, hydrogen bonding, disulfide bonding and possibly metal coordination structuring them. Also, the proteins are *not* in a collapsed, globular state, corresponding to $\upsilon = 0.38$ [31], as they are known to be disordered or with disordered sections [14]; thus the value of υ is limited to the range 0.4–0.588.

Table 1. Total number of amino acids (N) and molecular weights M.W. (Da) [32] after signal peptide cleavage as predicted by the SignalP v. 4.1 server [33], followed by the excluded volume Flory radius of gyration $R_g^1 = R_0 N^{0.588}$ (nm) with $R_0 = 0.193$ nm [29,34] as predicted for proteins in dilute solutions. For comparison, $R_g^2 = R_0 N^{0.5}$ is listed. In the plaques, we expect $R_g < R_g^1$. M.W. estimates do not include post-translational modifications (e.g. phosphorylation, hydroxylation).

	Mytilus californianus					*Mytilus galloprovincialis*				
mfp (variant)	accession no.	N	M.W.	R_g^1	R_g^2	accession no.	N	M.W.	R_g^1	R_g^2
mfp-1(1)	AAY29131.1	712	82 809	9.2	5.1	Q27409.1	727	83 191	9.3	5.2
mfp-2	not characterized					Q25464.1	456	49 840	7.1	4.1
mfp-3(1/A)	AAY29124.1	47	5606	1.9	1.3	BAB16314.1	46	5589	1.8	1.3
mfp-4(1)	ABC84184.1	751	88 215	9.5	5.3	not characterized				
mfp-5	ABE01084.1	78	9023	2.5	1.7	AAS00463.1	76	8880	2.5	1.7
mfp-6(1)	ABC84186.1	99	11 580	2.9	1.9	not characterized				

Table 2. Summary of model fit parameters.

species	condition	R_g (nm)	ξ_1 (nm)	ξ_2 (μm)
Mytilus californianus	19°C	8.2 ± 0.3	78.8 ± 0.6	0.71 ± 0.01
	GuHCl	12.4 ± 0.5	81.9 ± 0.9	0.71 ± 0.01
	3.8°C	7.6 ± 0.4	40.9 ± 0.2	0.81 ± 0.01
Mytilus galloprovincialis	19°C	5.9 ± 0.2	73.2 ± 0.5	0.86 ± 0.01
	GuHCl	11.9 ± 0.4	82.1 ± 0.9	0.71 ± 0.01
	3.8°C	6.9 ± 0.4	48.3 ± 0.3	1.13 ± 0.02

Here, $v = 0.5$ is chosen as the most reasonable Flory exponent. Figure 4 and table 2 show the data, fits and best fit values.

For our data, the best fit R_g values are $R_g = 8.2 \pm 0.3$ nm for *M. californianus* and $R_g = 5.9 \pm 0.2$ nm for *M. galloprovincialis*. Good agreement between theory and experiment emerges between the best fit R_g values and the predicted ones from Flory theory $R_g = R_0 N^v$ (table 1). For the excluded volume exponent $v = 0.588$, $R_0 \approx 0.193$ nm has been reported for denatured proteins [29,34] in solution. We use the same R_0 estimate with $v = 0.5$ and observe that the best fit values fall within the predicted values for the largest known proteins as expected. The presence of smaller proteins is expected to reduce the overall R_g, however, new evidence for the presence of unidentified proteins and the highly connected nature of individual proteins, which may make them appear as larger units, may contribute to the higher experimental R_g. Additional sources of error are the intrinsically large signal-to-noise ratio in that regime and the strong dependency on v. Future solution SAXS of the sequenced mfps at different pH values would be helpful in quantifying the R_g and their disordered nature.

4. The robustness of the plaque structure

4.1. The network structure of denaturant-treated plaques

The attachment of a mussel to surfaces is a vital necessity for the animal and one so important that it dedicates a minimum of 10% of its metabolic energy to byssus maintenance [12,35]. A structure of such importance is expected to be resilient in architecture at all length scales, from molecular to micro- and macroscopic. Yet, ocean acidification and laboratory studies simulating it have shown considerable plaque weakening and failure at lower forces [36]. We tested the structural robustness of the plaques made at 19°C at the other end of the pH spectrum, using the strong organic base and well-known chaotropic protein denaturant GuHCl whose ionic nature [37] screens the interactions between charged amino acids causing protein denaturation. In fact, GuHCl in addition to 5% acetic acid is used to extract mfp-5 [38].

Neutron scattering of plaques immersed in the 6 M GuHCl/D_2O solution was impossible due to the excess of incoherent scattering from the concentrated GuHCl. To avoid it, plaques incubated in GuHCl were placed in D_2O 1 h before the SANS measurement. I_{coh} has a similar overall trend to that obtained by the natural plaques and is well fitted by the modified DAB model (equation (3.1)) as shown in figure 6, demonstrating the lack of large structural changes, such as the collapse of the mesh network or pores. For both species, the best fit R_g^{Gu} almost doubles compared to the native values (table 2), reflecting the increased local disordering due to GuHCl. In contrast, the ξ_1^{Gu} values increase by 4% and 12% for *M. californianus* and *M. galloprovincialis*, respectively, while ξ_2^{Gu} remains similar. The larger effect of GuHCl on the molecular conformation (R_g) compared to the microstructure (ξ_1) showcases the stability and robustness of the network's architecture and organization to environmental conditions, in particular chemical degradation, and its independence from individual proteins. This conclusion is corroborated by the SEM images (figure 5*a–c*), which reveal that the mesh network as well as the network located

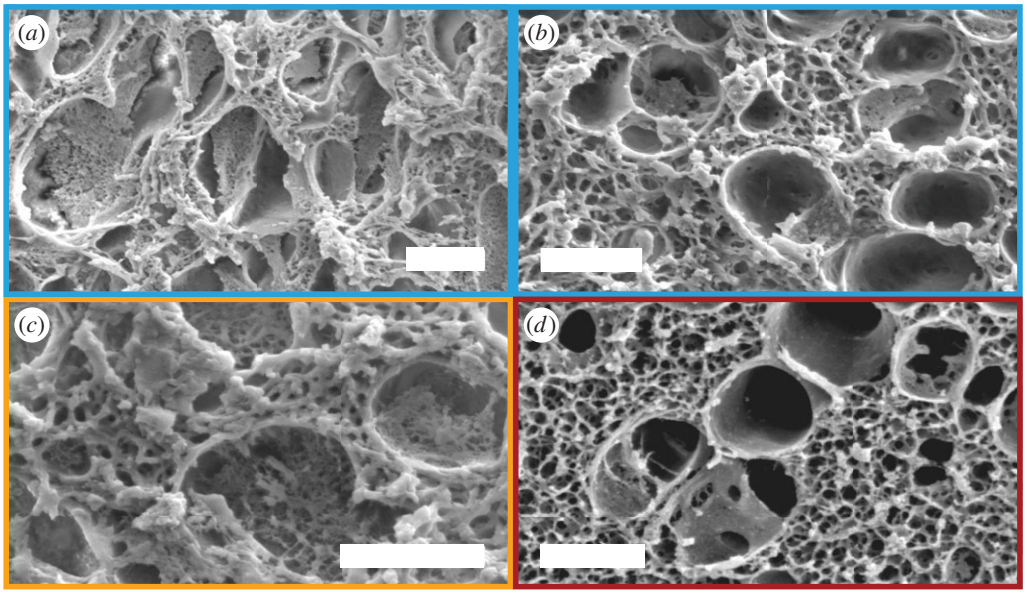

Figure 5. Representative SEM images of (*a*,*b*) *M. californianus* and (*c*) *M. galloprovincialis* plaques after treatment with 6 M GuHCl and replacement with water. (*d*) SEM of *M. californianus* plaque formed at 3.8°C. The struts of the mesh network are considerably thinner than the ones of the network of the 19°C plaques. Scale bar, 2 µm. (Online version in colour.)

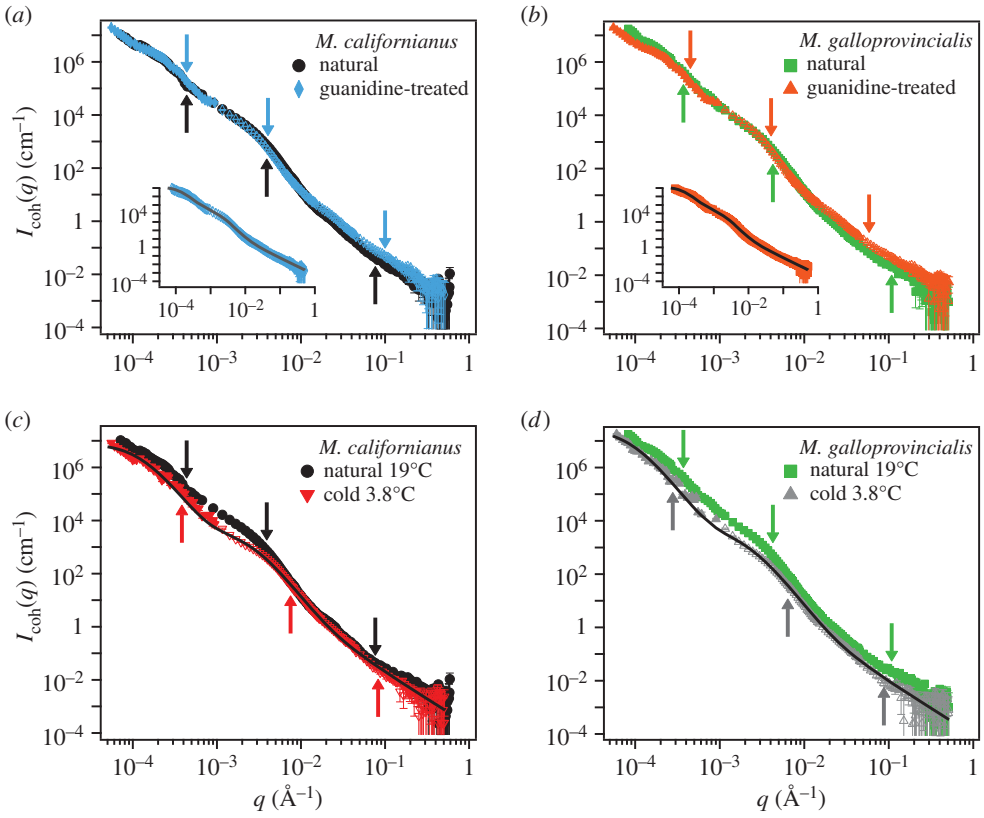

Figure 6. SANS ($0.001 < q < 0.58$ Å^{-1}) and USANS ($7 \times 10^{-5} < q < 9 \times 10^{-4}$ Å^{-1}) scattering intensity and model fit (solid lines) for the (*a*,*c*) *M. californianus* and (*b*,*d*) *M. galloprovincialis* plaques. Arrows (from left to right) indicate π/ξ_2, π/ξ_1 and $2\pi/R_g$. (*a*,*b*) Plaques made at 19°C, treated with guanidine hydrochloride in D_2O which was replaced with D_2O prior to measurement. The value of ξ_1 does not vary significantly. (*c*,*d*) Comparison of natural plaques made at 19°C with those made at 3.8°C. The value of ξ_1 is shifted to lower values. (Online version in colour.)

inside the pores are intact, despite the expectation that chemical degradation could have disrupted or collapsed them. Interestingly, mechanical processing such as freeze-drying is more destructive to the network. Clearly, we cannot exclude the possibility that the denaturation effects of days of immersion in GuHCl could have been partially reversed upon its removal and immersion in D_2O prior to scattering or preparation for SEM. However, even the possibility of a reversible change in structure points to the resilience of the mesh network against chemical degradation.

4.2. The network structure of plaques near freezing temperatures

The observation of the processing and kinetics of mussel thread and plaque formation is extremely difficult due to the muscular

tissue of the foot surrounding the ventral pedal groove. As an indirect probe, we attempted to perturb the kinetics of plaque formation using temperature as a control parameter. As ectothermic organisms, mussels adopt the water temperature. Seawater temperature in the area fluctuates between 16 and 18°C from June to August [39], the time mussels were collected for this experiment. We hypothesized that placing mussels at 3.8°C would slow down plaque formation, resulting in fewer or incomplete plaques or plaques with altered structure, possibly arrested at an earlier stage as kinetics, diffusion and phase transitions all depend on temperature. Biologically, this is another test of the robustness of plaque structure.

The mussels produce fewer, yet functional plaques. In handling the plaques however, we find the cold-formed plaques to be softer and more deformable than the typical 'natural' plaques formed at 19°C. Initial observation of SEM images of cold-formed plaques showed the same general structures observed for natural plaques: large pores containing a thin internal network, dispersed in a continuous mesh network. However, careful examination reveals the struts of the mesh network to be thinner, in the range of 40–90 nm as compared with the 75–95 nm range for the natural plaque struts. If this network has a load-bearing capacity and contributes to the plaque stiffness and strength, thinning its struts would be expected to weaken the overall plaque, in agreement with our qualitative observations of plaque mechanics during normal handling. Further mechanical experiments are necessary to quantify and confirm this correlation.

Scattering studies are extremely illuminating in this case. As shown in figure 6*c*,*d*, I_{coh} for natural versus cold-formed plaques differs in the vicinity of ξ_1 in the mid-q range. Best fits to the model (3.1) (table 2) result in $\xi_1^{cold} \approx 0.6\xi_1^{19°C}$. The lowest-$q$ regime is again increasing and the high-q regime agree within experimental uncertainty. To our knowledge, this is the first time that the temperature during plaque formation has been linked to plaque structure and in particular to a thinning of the mesh network. It is currently unclear whether plaque deposition is faster or slower in the cold waters, or whether reduced molecular diffusion crucially affects plaque formation. Other possibilities include slower chemical kinetics of mfp mixing, a shift in coacervation conditions or reduced solubility of the molecules. This novel view of the strong effect of temperature is guiding future experiments to decouple the roles such processes play in plaque formation.

5. The structure of induced plaques

To investigate whether the network and pore structures are self-assembled or whether the mussel actively controls the timing and sequence of protein secretions to form the network structure, we take advantage of the process of plaque induction using KCl injection at the pedal ganglion [15]. In this context, self-assembly is the equilibrium spontaneous process of forming an organized structure, the foam pattern, from the disordered components, the secretions of proteins. That is in contrast to 'processing' in which the final structure depends on the temporal sequence of component addition externally controlled by the mussel. The plaque induction experiment has environmental conditions similar to those of natural plaque formation. Prior studies [11,40] have confirmed that the induced and natural plaque secretions create acidic environments and are indistinguishable in terms of available proteins and to a certain extent their proportions. Therefore, plaque induction may differentiate between self-assembly and 'processing'. A result proving self-assembly could have important implications for the synthetic reconstruction of the plaques and the creation of porous materials. The induced plaque collection at three different time points (0, 10 and 30 min) and the immersion in seawater were used to probe temporal changes in the structure, such as self-organized spatial segregation of the pores, phase inversion from a liquid to a gel network or liquid–liquid phase separation arising from coacervation [21].

In all cases, the scattering obtained from induced plaques lacks any characteristic features. Rather they exhibit $I_{coh}(q) \sim q^{-3}$ for the entire USANS and SANS regimes, indicating a dense structure that lacks any dominant length scale. Figure 7*a* shows that the results from different time points are indistinguishable from each other, yet different from the scattering for the natural plaques shown in 7*b*. The scattering data obtained at different time points after immersion of the induced plaques to alkaline seawater look identical to the non-immersed ones (electronic supplementary material, figure S3). The fit, which is dominated by q^{-4}, unsurprisingly fails to converge to the data. The lack of pores and mesh network as they appeared in the natural or cold plaques is confirmed from the SEM images (figure 8), with the closest structure resembling pores appearing in figure 8*b*.

Both scattering and SEM results suggest that self-assembly is *not* the dominant route by which the plaque is created. The results indicate that temporal sequencing is in fact required for the specific structure observed in the native, non-induced plaques and the presence alone of the proteins is not sufficient to form the complex structure found in natural plaques. It is possible that differences in the pH, ionic strength and available salts in the induced case perturb the system, creating conditions unfavourable for self-assembly.

Finally, the self-assembly model of plaque proteins raises concerns about the temporal and spatial involvement of catechol oxidase, which is widely regarded as the cross-linking enzyme in mature natural plaques [13]. Although induced plaques appear to be largely uncross-linked, structure formation in load-bearing proteins (e.g. fibrin, collagen, elastin, keratin, etc.) typically precedes cross-linking.

6. Conclusion

We have demonstrated that the plaques of *M. californianus* and *M. galloprovincialis* are composed of a mesh network matrix into which larger pores are interdispersed with walls directly connected to the matrix. In contrast to previously held views of the plaque architecture [12], using a gentle solvent exchange preparation method for SEM we show that the mesh network is not a collapsed structure, but resembles an open-cell, reticulated foam. Large pore diameters fall in the 1–2 μm range and walls and matrix struts have a thickness of approximately 80 nm in the case of 19°C which reduces to almost half at 3.8°C, implicating for the first time temperature in plaque structure formation. The length scales of the structure are quantitatively confirmed by SANS and USANS measurements. We also show that the larger pores contain a network, which was previously destroyed upon freeze-drying. This new view of the plaque architecture has important implications regarding the understanding of load bearing and force distribution in the plaque, and the effect

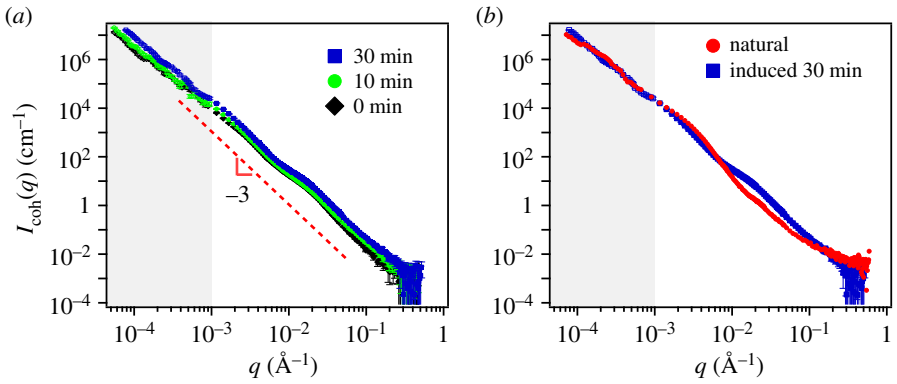

Figure 7. SANS and USANS (grey) scattering intensity for the *M. californianus* induced plaques (*a*) at different waiting times after the appearance of the first secretion (black diamond 0 min, green circle 10 min, blue square 30 min). (*b*) Comparison between the natural and the induced plaque with the longest waiting time. The model equation (3.1) fails to converge to the induced plaque $I_{coh}(q)$. (Online version in colour.)

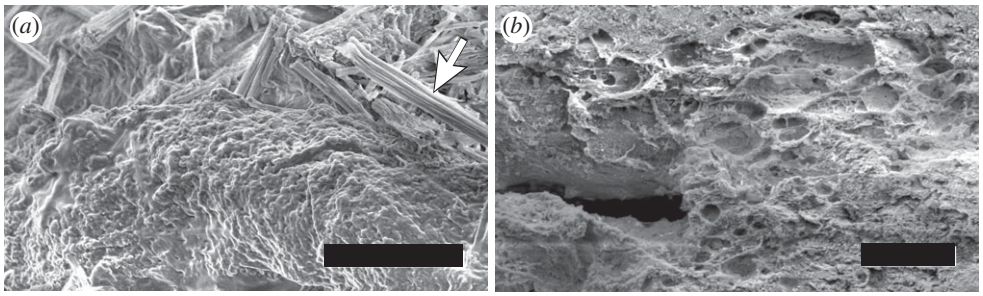

Figure 8. Representative SEM of induced plaques collected at (*a*) 0 min after first appearance of a secretion, showing a combination of granules reminiscent of the cuticle structure. Collagenous thread parts, which show ordering, were sectioned along with the plaque, since it is particularly hard to handle these soft secretions to separate plaque and thread. (*b*) At 30 min, structures resembling pores are appearing, surrounded by a dense nano-porous interior. Despite this evolution, the structure does not resemble the natural plaque. Scale bar, 10 µm.

of temperature to the mechanics. The examination of the mechanics will be the focus of future work.

Our results further demonstrate that the plaque is not degraded by standard denaturing conditions, likely due to the highly cross-linked nature of the proteins participating in plaque formation. We also determine that plaque structures do not self-assemble and show that despite the protein similarity in induced and natural plaques, the structures differ significantly. Future work will examine the temporal evolution of natural plaque formation.

Finally, the new insight we have gained into the microscopic structure of the mussel plaque provides the first step in both understanding and modelling the mechanics of mussel plaques and sets the stage for comparisons to other mussel species. Our results on natural plaques guide the creation of bioinspired synthetic adhesives with porous architecture with the goal of improving toughness under water just as the mussels do.

Data accessibility. Scattering data are deposited in the Dryad data repository (http://dx.doi.org/10.5061/dryad.mb580).

Authors' contributions. E.F. carried out the sample preparation, neutron scattering, electron microscopy, analysed the data and drafted the manuscript; D.D.M. and E.D. contributed to sample preparation, electron microscopy and drafting the manuscript; P.M.M. contributed to scattering data analysis; J.K. contributed to sample preparation and collection of neutron scattering data; M.H., H.W. and M.V. conceived and advised the study and edited the manuscript; H.W. additionally prepared samples. All authors gave final approval for publication.

Competing interests. The authors have no competing interests.

Funding. E.F. was supported by the MRSEC Program of the National Science Foundation under award no. DMR-1121053. D.D.M., E.D. and H.W. were supported by the National Institutes of Health grant no. R01-DE018468. P.M.M. and M.H. were supported by the Defense Threat Reduction Agency under the Natick Soldier Research, Development and Engineering Center agreement no. W911QY-13-2-0001. J.K. was supported by the National Science Foundation under award no. CBET 1351371. M.T.V. was partially supported by the Burroughs Wellcome Fund.

Acknowledgements. This work was supported by the MRSEC Program of the National Science Foundation under award no. DMR-1121053. We acknowledge the use of the NRI-MCDB Microscopy Facility at UCSB and the support of the National Institute of Standards and Technology, US Department of Commerce, in providing the neutron facilities used in this work. This work used facilities (BT5 USANS) supported in part by the National Science Foundation under agreement no. DMR-0944772.

References

1. Carrington E, Moeser GM, Dimond J, Mello JJ, Boller ML. 2009 Seasonal disturbance to mussel beds: field test of a mechanistic model predicting wave dislodgment. *Limnol. Oceanogr.* **54**, 978–986. (doi:10.4319/lo.2009.54.3.0978)
2. Lee H, Lee BP, Messersmith PB. 2007 A reversible wet/dry adhesive inspired by mussels and geckos. *Nature* **448**, 338–341. (doi:10.1038/nature05968)
3. Zhong C, Gurry T, Cheng AA, Downey J, Deng Z, Stultz CM, Lu TK. 2014 Strong underwater adhesives made by self-assembling multi-protein nanofibres. *Nat. Nanotechnol.* **9**, 858–866. (doi:10.1038/nnano.2014.199)
4. Meredith HJ, Jenkins CL, Wilker JJ. 2014 Strong underwater adhesives made by self-assembling multi-protein nanofibres. *Adv. Funct. Mater.* **24**, 3259–3267. (doi:10.1002/adfm.201303536)

5. Brubaker CE, Kissler H, Wang L-J, Kaufman DB, Messersmith PB. 2010 Biological performance of mussel-inspired adhesive in extrahepatic islet transplantation. *Biomaterials* **31**, 420–427. (doi:10.1016/j.biomaterials.2009.09.062)
6. Mehdizadeh M, Weng H, Gyawali D, Tang L, Yang J. 2012 Injectable citrate-based mussel-inspired tissue bioadhesives with high wet strength for sutureless wound closure. *Biomaterials* **33**, 7972–7983. (doi:10.1016/j.biomaterials.2012.07.055)
7. Qin Z, Buehler MJ. 2013 Impact tolerance in mussel thread networks by heterogeneous material distribution. *Nat. Commun.* **4**, 1–8. (doi:10.1038/ncomms3187)
8. Desmond KW, Zacchia NA, Waite JH, Valentine MT. 2015 Dynamics of mussel plaque detachment. *Soft Matter* **11**, 6832–6839. (doi:10.1039/C5SM01072A)
9. Meadows PS, Shand P. 1989 Experimental analysis of byssus thread production by *Mytilus edulis* and *Modiolus modiolus* in sediments. *Mar. Biol.* **101**, 219–226. (doi:10.1007/BF00391461)
10. Danner EW, Kan Y, Hammer MU, Israelachvili JN, Waite JH. 2012 Adhesion of mussel foot protein mefp-5 to mica: an underwater superglue. *Biochemistry* **51**, 6511–6518. (doi:10.1021/bi3002538)
11. Yu J, Wei W, Danner EW, Ashley RK, Israelachvili JN, Waite JH. 2011 Mussel protein adhesion depends on interprotein thiol-mediated redox modulation. *Nat. Chem. Biol.* **7**, 588–590. (doi:10.1038/nchembio.630)
12. Lee BP, Messersmith PB, Israelachvili JN, Waite JH. 2011 Mussel-inspired adhesives and coatings. *Annu. Rev. Mater. Res.* **41**, 99–132. (doi:10.1146/annurev-matsci-062910-100429)
13. McDowell LM, Burzio LA, Waite JH, Schaefer J. 1999 Rotational echo double resonance detection of cross-links formed in mussel byssus under high-flow stress. *J. Biol. Chem.* **274**, 20 293–20 295. (doi:10.1074/jbc.274.29.20293)
14. Hwang DS, Waite JH. 2012 Three intrinsically unstructured mussel adhesive proteins, mfp-1, mfp-2, and mfp-3: analysis by circular dichroism. *Protein Sci.* **21**, 1689–1695. (doi:10.1002/pro.2147)
15. Tamarin A, Lewis P, Askey J. 1976 The structure and formation of the byssus attachment plaque in *Mytilus*. *J. Morphol.* **149**, 199–221. (doi:10.1002/jmor.1051490205)
16. Kline SR. 2006 Reduction and analysis of SANS and USANS data using IGOR Pro. *J. Appl. Cryst.* **39**, 895–900. (doi:10.1107/S0021889806035059)
17. Bressler I, Kohlbrecher J, Thünemann AF. 2015 SASfit: a comprehensive tool for small-angle scattering data analysis. (http://arxiv.org/abs/1506.02958)
18. Nordestgaard BG, Rostgaard J. 1985 Critical-point drying versus freeze drying for scanning electron microscopy: a quantitative and qualitative study on isolated hepatocytes. *J. Microsc.* **137**, 189–207. (doi:10.1111/j.1365-2818.1985.tb02577.x)
19. Bray DF, Bagu J, Koegler P. 1993 Comparison of hexamethyldisilazane (HMDS), Peldri II, and critical-point drying methods for scanning electron microscopy of biological specimens. *Microsc. Res. Tech.* **26**, 489–495. (doi:10.1002/jemt.1070260603)
20. Michailidis N, Stergioudi F, Omar H, Tsipas DN. 2008 Investigation of the mechanical behavior of open-cell Ni foams by experimental and FEM procedures. *Adv. Eng. Mater.* **10**, 1122–1126. (doi:10.1002/adem.200800152)
21. Wei W, Tan Y, Martinez Rodriguez NR, Yu J, Israelachvili JN, Waite JH. 2014 A mussel-derived one component adhesive coacervate. *Acta Biomater.* **10**, 1663–1670. (doi:10.1016/j.actbio.2013.09.007)
22. Zheden V, von Byern J, Kerbl A, Leisch N, Staedler Y, Grunwald I, Power AM, Klepal W. 2012 Morphology of the cement apparatus and the cement of the buoy barnacle *Dosima fascicularis* (Crustacea, Cirripedia, Thoracica, Lepadidae). *Biol. Bull.* **223**, 192–204.
23. Stewart RJ, Weaver JC, Morse DE, Waite JH. 2004 The tube cement of *Phragmatopoma californica*: a solid foam. *J. Exp. Biol.* **207**, 4727–4734. (doi:10.1242/jeb.01330)
24. Wang CS, Stewart RJ. 2013 Multipart copolyelectrolyte adhesive of the sandcastle worm, *Phragmatopoma californica* (Fewkes): catechol oxidase catalyzed curing through peptidyl-DOPA. *Biomacromolecules* **14**, 1607–1617. (doi:10.1021/bm400251k)
25. Foster T, Safran SA, Sottmann T, Strey R. 2007 Scattering form factors for self-assembled network junctions. *J. Chem. Phys.* **127**, 204711. (doi:10.1063/1.2748754)
26. Hammouda B. 2012 Small-angle scattering from branched polymers. *Macromol. Theory Simul.* **21**, 372–381. (doi:10.1002/mats.201100111)
27. Shibayama M. 1998 Spatial inhomogeneity and dynamic fluctuations of polymer gels. *Macrom. Chem. Phys.* **199**, 1–30. (doi:10.1002/(SICI)1521-3935(19980101)199:1<1::AID-MACP1>3.0.CO;2-M)
28. Nie J, Du B, Oppermann W. 2004 Influence of formation conditions on spatial inhomogeneities in poly(*N*-isopropylacrylamide) hydrogels. *Macromolecules* **37**, 6558–6564. (doi:10.1021/ma049169d)
29. Kohn JE *et al.* 2004 Random-coil behavior and the dimensions of chemically unfolded proteins. *Proc. Natl Acad. Sci. USA* **101**, 12 491–12 496. (doi:10.1073/pnas.0403643101)
30. Le Guillou JC, Zinn-Justin J. 1977 Critical exponents for the n-vector model in three dimensions from field theory. *Phys. Rev. Lett.* **39**, 95–98. (doi:10.1103/PhysRevLett.39.95)
31. Millett IS, Doniach S, Plaxco KW. 2002 Toward a taxonomy of the denatured state: small angle scattering studies of unfolded proteins. *Adv. Protein Chem.* **62**, 241–262. (doi:10.1016/S0065-3233(02)62009-1)
32. National Center for Biotechnology Information protein database. 2014 See www.ncbi.nlm.nih.gov/protein/?term=foot+protein+mytilus.
33. Petersen TN, Brunak S, von Heijne G, Nielsen H. 2011 SignalP 4.0: discriminating signal peptides from transmembrane regions. *Nat. Methods.* **8**, 785–786. (doi:10.1038/nmeth.1701)
34. Kohn JE, Millett IS, Jacob J, Zagrovic B, Dillon TM, Cingel N *et al.* 2005 Correction for Kohn *et al.*, Random-coil behavior and the dimensions of chemically unfolded proteins, *PNAS* 2004 101:12491-12496. *Proc. Natl Acad. Sci. USA* **102**, 14475. (doi:10.1073/pnas.0507472102)
35. Griffiths CL, King JA. 1979 Energy expended on growth and gonad output in the ribbed mussel *Aulacomya ater*. *Mar. Biol.* **53**, 217–222. (doi:10.1007/BF00952429)
36. O'Donnell MJ, George MN, Carrington E. 2013 Mussel byssus attachment weakened by ocean acidification. *Nat. Clim. Change* **3**, 587–590. (doi:10.1038/nclimate1846)
37. Monera OD, Kay CM, Hodges RS. 1994 Protein denaturation with guanidine hydrochloride or urea provides. *Protein Sci.* **3**, 1984–1991. (doi:10.1002/pro.5560031110)
38. Zhao H, Waite JH. 2006 Linking adhesive and structural proteins in the attachment plaque of *Mytilus californianus*. *J. Biol. Chem.* **281**, 26 150–26 158. (doi:10.1074/jbc.M604357200)
39. National Oceanic and Atmospheric Administration. 2015 Water temperature table of the South Pacific Coast. See www.nodc.noaa.gov/dsdt/cwtg/spac.html.
40. Martinez Rodriguez NR, Das S, Kaufman Y, Israelachvili JN, Waite JH. 2015 Interfacial pH during mussel adhesive plaque formation. *Biofouling* **31**, 221–227. (doi:10.1080/08927014.2015.1026337)